Chinese Chemical Letters 35 (2024) 109537

Contents lists available at ScienceDirect

Chinese Chemical Letters

journal homepage: www.elsevier.com/locate/cclet

Utilizing dual-responsive iridium(III) complex for hepatocellular carcinoma: Integrating photoacoustic imaging with chemotherapy and photodynamic therapy

Jinyu Guo[a,b,1], Yandai Lin[b,1], Shaohua He[d,1], Yueqing Chen[a,b], Fenglu Li[b], Renjie Ruan[a], Gaoxing Pan[b], Hexin Nan[c], Jibin Song[c], Jin Zhang[a,b,*]

[a] Qingyuan Innovation Laboratory, Quanzhou 362801, China
[b] College of Chemical Engineering, Fuzhou University, Fuzhou 350108, China
[c] MOE Key Laboratory for Analytical Science of Food Safety and Biology, State Key Laboratory of Photocatalysis on Energy and Environment, College of Chemistry, Fuzhou University, Fuzhou 350108, China
[d] Department of Pediatric Surgery, Shengli Clinical Medical College of Fujian Medical University, Fuzhou 350001, China

ARTICLE INFO

Article history:
Received 8 November 2023
Revised 16 January 2024
Accepted 17 January 2024
Available online 20 January 2024

Keywords:
Amphiphilic iridium complex
Transferrin targeting
NIR/GSH dual-responsiveness
Photoacoustic imaging
Synergistic tumor therapy

ABSTRACT

Stimuli-triggered release and alleviating resistance of iridium(III)-based drugs at tumor sites remains challengeable for clinical hepatoma therapy. Herein, a doxorubicin@iridium-transferrin (DOX@Ir-TF) nanovesicle was synthesized by carboxylated-transferrin (TF) and doxorubicin-loaded amphiphilic iridium-amino with quaternary ammonium (QA) groups and disulfide bonds. The QA groups enhanced photophysical properties and broadened production capacity of photoinduced-reactive oxygen species (ROS), while the disulfide-bridged bonds regulated oxidative stress levels through reacting with glutathione (GSH); simultaneously, modification of TF improved recognition and endocytosis of the nanovesicle for tumor cells. Based on *in-vitro* results, a controlled-release behavior of DOX upon a dual-responsiveness of GSH and near-infrared ray (NIR) irradiation was presented, along with high-efficiency generation of ROS. After an intravenous injection, the nanovesicle was targeted at tumor sites, realizing TF-navigated photoacoustic imaging guidance and synergistic chemotherapy-photodynamic therapy under NIR/GSH stimulations. Overall, newly-synthesized DOX@Ir-TF nanovesicle provided a potential in subcutaneous hepatocellular carcinoma therapy due to integrations of targeting delivery, dual-stimuli responsive release, synergistic therapy strategy, and real-time monitoring.

Hepatocellular carcinoma, predominantly asymptomatic in early stages, often leads to late diagnosis, high relapse rates, and poor prognosis [1]. Conventional treatments such as surgery, chemotherapy, and photodynamic therapy (PDT) are not highly efficient when used in isolation [2]. Synergistic therapies of combining chemotherapy with PDT, particularly using nanoplatforms, are gaining attention. For instance, a nanocomposite of zinc phthalocyanine, sorafenib, and bovine serum albumin achieved inhibition of hepatocellular carcinoma growth through launching a highly-efficient chemo-, PDT-, and photothermal-therapy upon an irradiation [3]. Photosensitizers in PDT, especially the cyclometalated iridium (Ir)-based complex, are explored for hepatocellular carcinoma treatment due to their ability to generate cytotoxic reactive oxygen species (ROS) with minimal invasiveness and high precision [4]. The Ir complex, notable for its photochemical stability and photophysical properties, effectively produces both oxygen-independent type I ROS like superoxide anion radical ($O_2^{\bullet-}$) and oxygen-dependent type II ROS such as singlet oxygen ($^1O_2$), obviously-alleviating hypoxia-related limitations in tumor treatment [5]. Despite these merits, applications of these Ir-based complexes are hindered by challenges comprising poor performance, low targeting ability, and limited stimuli-responsiveness [5,6].

Quaternary ammonium (QA) as a hydrophilic moiety, is modified cyclometalating ligands (ĈN) and auxiliary ligands (NN̂) of hydrophobic transition metal complexes. Particularly, it tuned photophysical or/and electrochemical characteristics of the complexes by altering charge redistribution and maintaining dynamic equilibrium within the principal frameworks. These modifications increase solubility and endocytosis efficiency of cyclometalated Ir-based complexes while reducing fluorescence aggregation-caused

* Corresponding author.
E-mail address: J_zhang929@fzu.edu.cn (J. Zhang).
[1] These authors contributed equally to this work.

https://doi.org/10.1016/j.cclet.2024.109537
1001-8417/

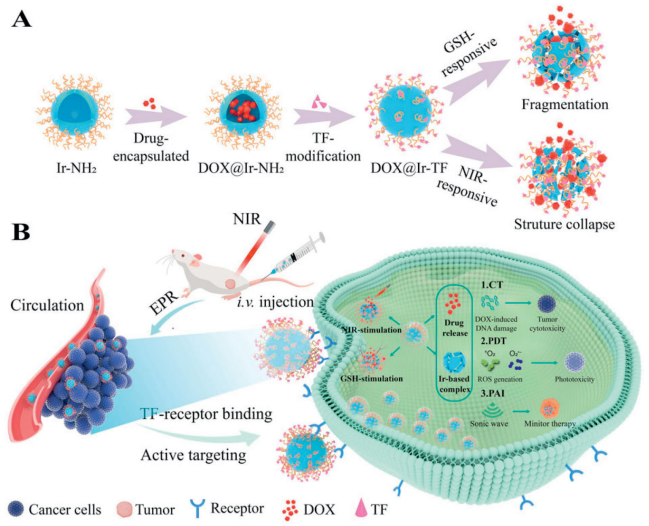

Fig. 1. Schematic illustration of (A) synthesis route and (B) intravenous (i.v.) injection of DOX@Ir-TF nanovesicle for PAI-guided synergistic chemotherapy/PDT of hepatocellular carcinoma.

quenching by diminishing π-π stacking probability [7]. Further enhancements involve modifying these complexes with transferrin (TF), which targets malignant cells with overexpressed TF receptors, thus facilitating receptor-mediated endocytosis and guiding PDT towards the self-assembled nanovesicles [8]. Precisely-targeting tumor site of these nanovesicles raises question of the controlled drug release, a crucial factor in antitumor efficiency [9,10]. The exogenous stimulus of near-infrared ray (NIR) irradiation, alongside prevalent existing of glutathione (GSH) in tumor cells, are key in triggering drug release and enhancing ROS generation [11]. In this context, the synthesized Ir-based complex with NIR/GSH dual-responsiveness is expected to optimize drug delivery and efficacy at tumor sites.

To address the requirements of targeting endocytosis, controlled delivery, and amplified therapy efficiency, a newly-engineered doxorubicin@iridium-transferrin (DOX@Ir-TF) nanovesicle was fabricated herein by loading DOX and conjugating carboxylated-TF onto an amphiphilic iridium-amino (Ir-NH_2) complex with QA groups and disulfide-bridged bonds (Fig. 1A). Cell assays revealed that the DOX@Ir-TF nanovesicle owned specific targeting towards cytomembranes and efficient cellular uptake. *In-vivo* studies proved their prominent anticancer activity and remarkable inhibition performance under synergistic effect of chemotherapy/PDT, where a highly-efficient generation of ROS and controlled release of chemotherapy drug were realized upon local NIR/GSH stimuli after an intravenous injection (Fig. 1B). More interestingly, our synthesized DOX@Ir-TF nanovesicle presented impressive photoacoustic imaging (PAI) capability, aiding in monitoring material disintegration *in vivo* and achieving rapid pathological analysis or diagnosis of tumors.

Synthesis process, physical performance characterizations, and *in vitro*/*in vivo* evaluations of the DOX@Ir-TF nanovesicle were described in Supporting information. All procedures performed in studies involving mice were in accordance with the Animal Ethics Committee of Fujian Medical University (Approval No. 2017–070, Fuzhou, China) and were strictly performed according to the National Institutes of Health Guide for the Care and Use of Laboratory Animals (1996).

Multifunctional Ir-based complexes have exhibited high fluorescence quantum yields in solution, but their fluorescence intensity may be affected by aggregation states. Integrations of hexadecyldimethylamine and QA into the Ir-NH_2 complex first overcame aggregation by increasing the hydrophilicity. This modification ensured a bilayer core formation with symmetrically-aligned aromatic entities and parallel alkyl chains as hydrophobic tails, so as to minimize π-π interactions, reduce nonradiative energy transfer, and inhibit fluorescence quenching of the aggregated Ir-based complexes [12]. Detailed synthesis routes of the resultant Ir-NH_2 complex were shown in Fig. S1 (Supporting information) and Fig. 2A. Specifically, a hydrophobic end containing cetyl quaternary ammonium salt was provided to load DOX based on hydrophobic interactions *via* hydrogen bonds and intermolecular hydrophobic stack. Meanwhile, a hydrophilic end containing disulfide bonds and cystamine dihydrochloride was used to realize GSH-responsiveness and bind with carboxylated-TF *via* amide reactions, separately. Structural verifications and descriptions of intermediate products and Ir-NH_2 complex were described in Supporting information (Figs. S2–S6 in Supporting information).

Hydrogen atom numbers, parent ions, and related fragment ions of the Ir-NH_2 complex were confirmed by ^{1}H NMR (Fig. S7 in Supporting information) and ESI-HRMS/MS (Fig. S8 in Supporting information). Following mass spectrometry data, Fourier-transform infrared spectroscopy (FTIR) absorption bands appeared at 3100−2600 cm^{-1} were assigned to C−H stretching vibrations from the alkyl groups, and peaks located at 3300, 1643, and 1540 cm^{-1} were accordingly ascribed to stretching vibration models of N−H, C=O, and C=N groups, while C−N bending vibration (1290 cm^{-1}) was mainly caused by QA group in the synthesized Ir-NH_2 complex (Fig. 2B). Afterwards, the doxorubicin@iridium-amino (DOX@Ir-NH_2) nanovesicle was further constructed by encapsulation DOX within this dual-responsive Ir-NH_2 complex *via* hydrophobic interactions, hydrogen bonding, and intermolecular hydrophobic stacking. Thereafter, the carboxylated-TF was modified onto surface of the DOX@Ir-NH_2 complex *via* amide reactions to obtain the resultant targeting DOX@Ir-TF nanovesicle. Morphologies of the as-prepared Ir-NH_2, DOX@Ir-NH_2, and DOX@Ir-TF specimens were observed by TEM, in which situations all the specimens presented uniform spherical shapes (Fig. S9 in Supporting information). Following this, average sizes of the above specimens were measured and exhibited in Fig. S10 (Supporting information). Such a significant increase in nanoparticle sizes was ascribed to functionalization of DOX and TF, where the DOX was occupied spatially in hydrophobic core and the TF prolonged hydrophilic terminal domains [13]. Dynamic light scattering (DLS) analysis shown in Fig. S11 (Supporting information) echoed these findings, demonstrating good dispersion and stability of these specimens in deionized water. Despite larger hydrodynamic diameters attributed to agglomeration effects were revealed in DLS result [14], the consistency in experimental results was maintained across all the groups. Stability of the self-assembled DOX@Ir-TF nanovesicle in an aqueous solution was further affirmed through evaluation of polydispersity index (PDI) over six days (Fig. S12 in Supporting information), suggesting that existences of long alkyl chains and TF-enhanced amphiphilicity, form stable, and homogeneous nanovesicles [5,12].

Intramolecular charge transfer characteristics of the Ir-NH_2 complex were also investigated through electrostatic potential (ESP) analysis between its ground state (S_0) and the lowest singlet excited state (S_1) with a geometry optimization. As shown in Fig. 2C, the ESP was distributed across whole molecules of the Ir-NH_2 complex, unveiling homogenous carrier transporting properties. Electron-poor or positive ESP sites, concentrated at the Ir-based center, suggest a potential for charge transfer from a donor of ĈN ligands to NN̂ ligands upon external or internal stimuli [15]. Thereafter, density functional theory (DFT) analysis revealed the highest occupied molecular orbital (HOMO) primarily localized at ĈN ligands, and the lowest unoccupied molecular orbital (LUMO) at the Ir-based framework and NN̂ ligands, with corresponding HOMO and LUMO energy levels at −5.53 and −2.77 eV, respectively (Fig.

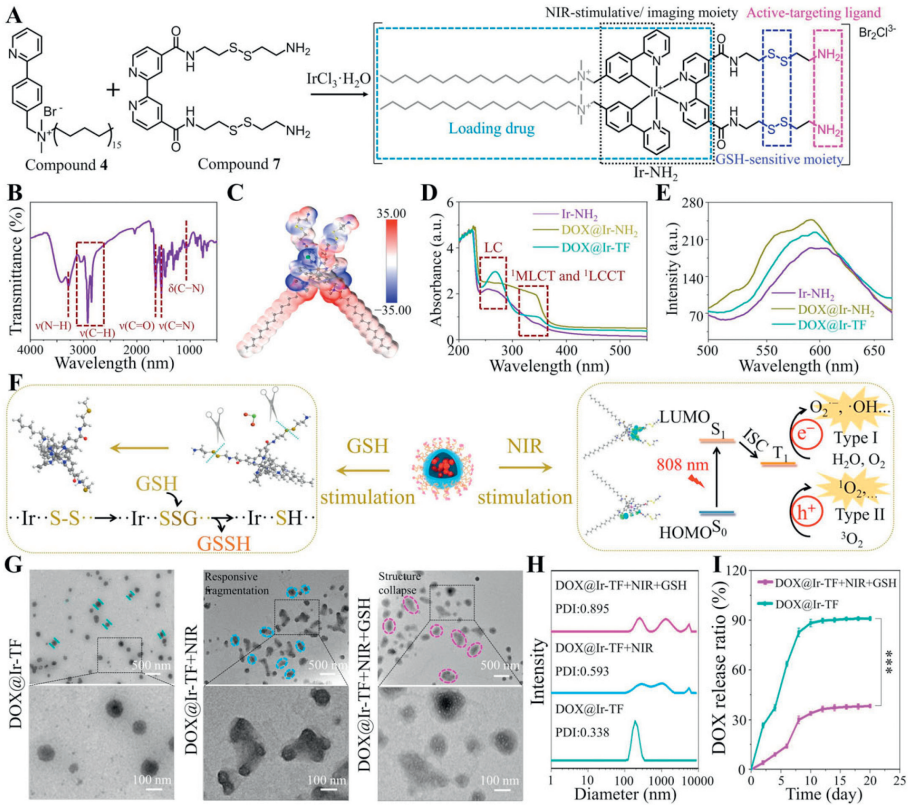

Fig. 2. Synthetic route and physical characterizations of different Ir-based complexes and NIR/GSH dual-responsiveness of DOX@Ir-TF. (A) Synthetic route, (B) FTIR analysis, and (C) ESP distributions of Ir-NH_2 complex with multifunctional moieties. Blue and red colors indicate low and high charge density, respectively. (D) UV–vis absorptions (LC, ligand-centered; ^{1}MLCT, metal-to-ligand charge transition; ^{1}LCCT, ligand-centered charge-transfer) and (E) fluorescence emission spectra of Ir-NH_2, DOX@Ir-NH_2, and DOX@Ir-TF specimens. (F) NIR/GSH dual-responsive mechanism of DOX@Ir-TF nanovesicle (GSSH, oxidized glutathione; GSH counterpart). (G) Representative TEM images and (H) DLS analyses of DOX@Ir-TF, DOX@Ir-TF+NIR, and DOX@Ir-TF+NIR+GSH samples. Scale bars: 500 nm and 100 nm. (I) Release profiles of DOX from DOX@Ir-TF nanovesicle with or without NIR/GSH dual-stimuli. All statistical data are presented as mean ± SD ($n = 3$; $^{***}P < 0.001$).

S13 in Supporting information). Distinct asymmetry in HOMO and LUMO distributions implied a propensity for charge-transfer upon activation by external stimuli, while electrons transferring from ĈN ligands moieties to the Ir-based main framework [16].

Intracellular endocytosis of the nanovesicles was related to spherical surface charge, which enhanced tumor cell surface affinity [17]. As shown in Fig. S14 (Supporting information), the Ir-NH_2 complex had a large potential value of 65.57 ± 1.31 mV due to positively-charged QA groups and DOX incorporation. Conversely, zeta potentials of the DOX@Ir-NH_2 and DOX@Ir-TF samples were 18.60 ± 0.60 and −1.54 ± 0.59 mV, respectively, indicating successful loadings of negatively-charged DOX and TF. Such negative surface charge enhanced the DOX@Ir-TF nanovesicle's bloodstream circulation, promoting intracellular uptake and tumor site accumulation. Subsequently, ultraviolet–visible spectroscopy (UV–vis) absorptions showed characteristic absorption bands of the DOX@Ir-NH_2 and DOX@Ir-TF, maintaining in characteristic peaks of the Ir-NH_2 (Fig. 2D). This was indicative of the DOX@Ir-TF efficient light-harvesting ability and potential as a photosensitizer [15]. Upon 365 nm excitation, fluorescence emission spectrum of the DOX@Ir-TF nanovesicle exhibited a slight red shift compared to the DOX@Ir-NH_2 complex (Fig. 2E), ascribing to structural changes post-TF modification [18]. In brief, the DOX@Ir-TF nanovesicle inherited photophysical properties of the Ir-NH_2 complex, also embraced loading capacity of DOX and targeting ability of TF.

NIR/GSH dual-responsive mechanism of the DOX@Ir-TF nanovesicle was illustrated in Fig. 2F. Specifically, GSH functioning as a molecular "scissor", reduced disulfide bonds into thiol groups (–SH) and generated oxidized GSH [19]. This cleavage of disulfide bonds within the Ir-based complex acted as a release valve, compelling partial disintegration of the complex alongside gradual release of DOX. Structure of the Ir-based complex was further collapsed under NIR irradiation according to the DFT calculations conducted on a 6–311G** basis [20]. In detail, HOMO of the complex was mainly localized at the ĈN ligands from QA, while LUMO of the complex was localized at the cyclometalated Ir-based framework and NN̂ ligands from cystamine dihydrochloride. Distinct asymmetric distributions of HOMO and LUMO implied an occurrence of charge-transfer process and then induced generation of type I ROS because the Ir-based complex was activated by optical or electron stimulations. Additionally, a narrow band gap from the HOMO and LUMO (Fig. S13 in Supporting information) benefited for energy transfer process as well as type II ROS generation [16].

Controlled release of DOX within the DOX@Ir-TF nanovesicle was dependent on its NIR/GSH dual-responsiveness behaviors. Upon 808 nm laser irradiation for 5 min, size of the DOX@Ir-TF nanovesicle visually increased (Fig. 2G), indicating a NIR-responsive DOX leakage due to an accelerated intramolecular thermal movement of small-molecule drugs. Furthermore, the DOX@Ir-TF sample also presented a GSH-responsive DOX release, as evidenced by a dramatically-increased nanovesicle size in GSH solution with a concentration of 10.0 mmol/L. Disulfide bonds existed in the DOX@Ir-TF nanovesicle were sensitive to excessive GSH [9]. Breaking of the disulfide bond moieties interrupted an internal balance between hydrophilicity and hydrophobicity domains, so as to result in a disassembly of the nanovesicle and an exacerbated release of hydrophobic DOX. Hence, both NIR and GSH stimuli were

acted as valves for triggering controlled release of DOX from the DOX@Ir-TF nanovesicle through compelling intra-molecular movements as well as recombining hydrophilicity and hydrophobicity, respectively.

Consistent with qualitative results, average nanovesicle sizes in the DOX@Ir-TF, DOX@Ir-TF+NIR, and DOX@Ir-TF+NIR+GSH groups were 159.3 ± 2.7, 225.8 ± 10.0, and 287.2 ± 12.9 nm, respectively (Fig. S15 in Supporting information). PDI values of the DOX@Ir-TF also increased from 0.338 to 0.593 after 5 min of NIR irradiation, which then increased to 0.895 after immersing the nanovesicles in 10.0 mmol/L GSH solution (Fig. 2H). Such increased sizes, as well as PDI values, reflected NIR/GSH dual-responsive properties of the DOX@Ir-TF nanovesicle, where NIR and GSH were two important factors for synergistically disrupting intramolecular and intermolecular equilibrium of the nanovesicles. This was further corroborated by the DOX release behavior where different concentrations (0–70 μg/mL) loaded onto the Ir-NH_2 complex with an encapsulation efficiency of 32.5% ± 1.1% (Fig. S16 in Supporting information). Moreover, release rates of DOX at 20 days were significantly higher in the DOX@Ir-TF+NIR+GSH group (91.3% ± 1.3%) compared to the DOX@Ir-TF group (38.3% ± 0.9%) (Fig. 2I), demonstrating an enhancement of NIR/GSH responsiveness towards drug release.

UV–vis absorptions of the DOX@Ir-TF nanovesicle in both GSH absence and presence situations were shown in Fig. S17 (Supporting information). Obviously, absorbance of the nanovesicle at 266 nm disappeared along with breakage of the disulfide bonds after GSH stimulation, while broad absorption bands in ranges of 285–350 and 458–570 nm were emerged, demonstrating existences of the LC, ^{1}LCCT, and ^{1}MLCT [21]. This shift implied breakage of disulfide bonds from NN̂ ligands of the nanovesicle due to GSH stimulation. Meanwhile, ROS generation ability of the nanovesicle upon NIR irradiation was evaluated using 2′,7′-dichlorodihydrofluorescein diacetate (DCFH-DA), revealing a significant increase in fluorescence intensity with extended irradiation times (Fig. S18 in Supporting information). As a promising photosensitizer, the DOX@Ir-TF nanovesicle was highly probable to produce type I and II ROS for PDT enhancement. Electron spin resonance spectroscopy was then used to confirm types of ROS generated by the DOX@Ir-TF nanovesicle. Accordingly, tetramethylpiperidine and 5,5-dimethyl-1-pyrroline *N*-oxide (DMPO) were employed as $^1O_2$ and $O_2^{\bullet-}$ trappers, respectively [22]. Characteristic signals of the spin adduct (4-oxo-2,2,6,6-tetramethyl-1-piperidinyloxy) under light irradiation for the DOX@Ir-TF nanovesicle were displayed, manifesting of $^1O_2$ production (Fig. S19A in Supporting information). Accordant signals with spin adduct (2-hydroperoxy-5,5-dimethyl-1-pyrrolidinyloxyl) as a spin derivative of DMPO–$O_2^{\bullet-}$ were obtained (Fig. S19B in Supporting information), indicating it owned an ability to reduce O_2 to $O_2^{\bullet-}$ species. Above results collectively elaborated two types of ROS generations by the cyclometalated DOX@Ir-TF nanovesicle due to its structural configuration and QA-amplified intersystem crossing behavior. This makes the DOX@Ir-TF nanovesicle a dual-stimulative photo-dynamic agent, capable of disrupting cellular antioxidant defenses and regulating DOX release in tumor cells.

Cytotoxicity of the DOX@Ir-NH_2 and DOX@Ir-TF nanovesicles, indicative of their compatibility with living tissues, were investigated by cell counting kit-8 (CCK-8) test and LIVE/DEAD staining assay. Initial tests showed that both nanovesicles at concentrations ranging from 0.00 to 0.15 mg/mL, had negligible toxicity towards L02 cells (Fig. S20 in Supporting information). This favorable cytotoxicity profile was mainly ascribed to modifications of hydrophilic QA groups or/and TF, which enhanced dispersibility and biocompatibility of the nanovesicle. Further studies were conducted by co-culturing L02 cells without/with the DOX@Ir-TF nanovesicle at a concentration of 0.09 mg/mL over 1, 3, and 5 days. A LIVE/DEAD staining assay employed calcein acetoxymethyl ester (calcein-AM; green, live cells) and propidium iodide (PI; red, dead cells) reagents. Large number of live cells were observed from the 3rd day after incubation with the control and DOX@Ir-TF nanovesicles (Fig. S21 in Supporting information), and meanwhile, the cell viability and proliferation rate exhibited significantly-increasing trends along with time (Fig. S22 in Supporting information). These findings collectively demonstrated convincing biocompatibility of as-synthesized DOX@Ir-TF nanovesicle, laying a biological foundation for subsequent *in vivo* experiments.

A LIVE/DEAD staining assay was further employed to assess synergistic chemotherapy/PDT effect of the nanovesicles towards HepG2 cells, a widely-used cell line in hepatocellular carcinoma research due to its genetic stability and representativeness [23]. In control group, there were many live tumor cells (green) in the absence of NIR, and a few dead cells (red) were detectable due to GSH-stimulated DOX release (Fig. 3A). In contrast, a large number of dead tumor cells were discovered after treatment with the DOX@Ir-TF and DOX@Ir-NH_2 nanovesicles upon NIR irradiation and endogenous GSH stimulation. Interestingly, the DOX@Ir-TF nanovesicle induced more cell death than the DOX@Ir-NH_2 group under the same irradiation conditions, implying the TF targeting effect in enhancing therapy efficiency *in vitro*. Moreover, CCK-8 assay quantitatively demonstrated that the DOX@Ir-TF sample exhibited the highest cytotoxicity to HepG2 cells compared to the control and DOX@Ir-NH_2 groups (Fig. 3B). This increased efficacy from the DOX@Ir-TF was attributed to TF-navigated nanovesicle accumulation, effective ROS generation upon NIR irradiation, and NIR/GSH dual-responsive DOX release.

Effective intracellular absorption of the nanovesicles is prerequisite for determining synergistic chemotherapy/PDT effect [24]. Consequently, colocalization experiments with HepG2 cells being stained with blue for nuclei and red for experimental samples were conducted. Fluorescence intensity of the DOX@Ir-TF nanovesicle was noticeably higher than that of the DOX@Ir-NH_2 sample in HepG2 cells after 6 h, suggesting a stronger endocytosis effect (Fig. 3C and Fig. S23 in Supporting information). This was quantitatively confirmed by comparing the mean fluorescence intensity of the DOX@Ir-TF, which was about five times higher than that of the DOX@Ir-NH_2 group (Fig. 3D), underscoring enhanced cellular accumulation and uptake. Transferrin receptor 2 (TFR2), generally overexpressed in tumor cells, enhances transportation ability of the TF-modified Ir-based complexes into mitochondria *via* interactions between the exposed TF and TFR2 [25]. After recognizing and trapping TF on membranes of tumor cells, QA groups in nanovesicle framework have functioned as a reserve force to facilitate caveolae-mediated endocytosis production [26].

After assessments of cytotoxicity and cellular endocytosis of the DOX@Ir-TF nanovesicle, intracellular ROS generations inside HepG2 cells for different groups were also evaluated *in vitro* through DCFH-DA (green) and 4′,6-diamidino-2-phenylindole (DAPI; blue) co-staining fluorescence imaging experiments (Fig. 3F and Fig. S24 in Supporting information). Under NIR irradiation, HepG2 cells with incubations of the DOX@Ir-NH_2 and DOX@Ir-TF specimens exhibited intense green fluorescence, indicating robust ROS generation within these two specimens. A maximum ROS generation in the DOX@Ir-TF group was observed, ascribing to TF-navigating accumulation and NIR mediation effect. A quantitative analysis of mean fluorescence intensity from these confocal laser scanning microscopy (CLSM) images was summarized in Fig. 3E, which revealed that green fluorescence in the DOX@Ir-TF+NIR group was substantially higher than that in the control, DOX@Ir-NH_2, and DOX@Ir-TF, and DOX@Ir-NH_2+NIR groups. Noticeably, ROS production level in the DOX@Ir-TF+NIR group exceeded that in the DOX@Ir-NH_2+NIR group, being attributed to additional ROS generation resulting from protein misfolding subsequent to accumulation and uptake of the DOX@Ir-TF within tumor cells [27]. Be-

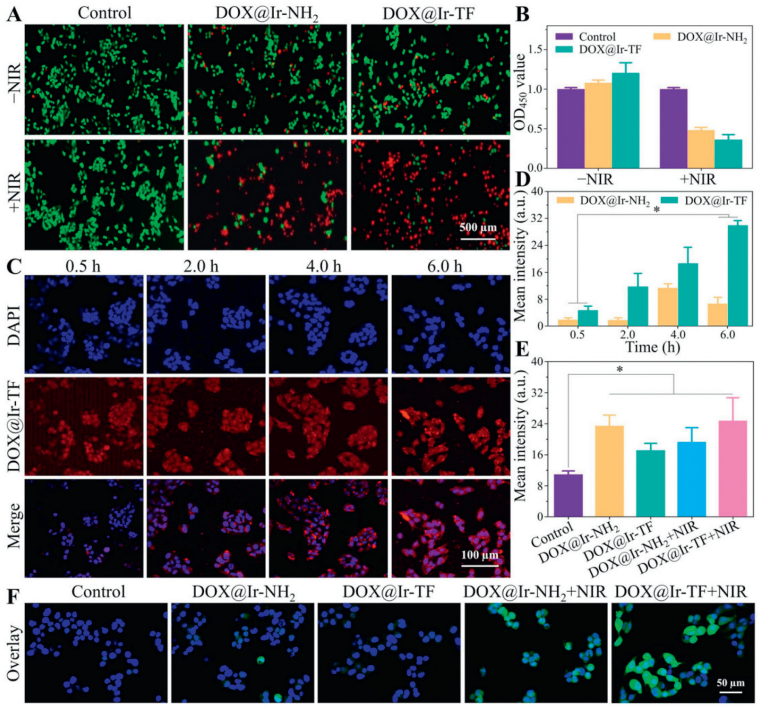

Fig. 3. Cytotoxicity, cellular endocytosis, and antitumor activity assessments of DOX@Ir-TF *in vitro*. (A) LIVE/DEAD staining images and (B) CCK-8 analyses of HepG2 cells in different groups with or without NIR irradiation. Scale bar: 500 μm. (C) Typical CLSM images and (D) quantitative analyses of HepG2 intracellular localization with increasing incubation time (cell nuclei: blue; DOX@Ir-TF nanovesicle: red). Scale bar: 100 μm. (E) Quantitative analyses and (F) representative CLSM images of intracellular ROS generation in different groups after being stained with DAPI and DCFH-DA. Scale bar: 50 μm. All statistical data are presented as mean ± SD ($n = 3$; $^*P < 0.05$).

sides, images containing green and blue fluorescence signals in the DOX@Ir-TF+NIR group were overlapped well, demonstrating that the ROS generation occurred within tumor cells and thus helpful to achieving antitumor effects by generated phototoxicity [5].

Biodegradability and pharmacokinetic behavior of the DOX@Ir-TF nanovesicle were further investigated *in vivo*. After an administration to mice, pharmacokinetic parameters of the nanovesicle were quantified and summarized in Fig. S25 and Table S1 (Supporting information) [28]. First, an elimination half-life time ($t_{1/2} = 15.72 \pm 5.58$ h) and a significant area under a curve ($AUC_{0\text{-}t} = 21{,}677.93 \pm 1169.99$ μg L^{-1} h) indicated a prolonged systemic circulation. This extended circulation was primarily attributed to surface charge, particle size, and amphiphilic structure of the DOX@Ir-TF. Then, metabolic processes were also assessed by analyzing iridium content from urine samples, which showed a peak concentration at 24 h post-injection and gradually decreased along with time (Fig. S26 in Supporting information). Overall, the DOX@Ir-TF nanovesicle presented an extended blood half-life, a favorable biodegradability along with a high biocompatibility.

In addition, *in vivo* antitumor therapy performance of the nanovesicles was further explored using Hepa1–6 cell model due to its high compatibility with biological milieu of mice, offering an efficient setting for subcutaneous hepatocellular carcinoma treatment [29]. Hence, subcutaneous Hepa 1–6 hepatocarcinoma cell-bearing BALB/c nude mice were randomly assigned into five groups and then intravenously injected with different nanovesicle solutions at predetermined intervals (1, 3, 5, 7, and 9 days) (Fig. 4A). Changes on tumor volumes and body weights were measured once for two days to evaluate the therapeutic effect. As the mice were euthanasia, representative photographs of tumors *ex vivo* after surgery were displayed (Fig. 4C), and visually, the lowest weights, smallest volumes, as well as lowest weight ratios (tumor weight/body weight) of the tumors were presented in the DOX@Ir-TF+NIR group (Figs. 4E and G, and Fig. S27 in Supporting information), demonstrating the DOX@Ir-TF nanovesicle's high NIR/GSH-mediated chemotherapy/PDT synergistic antitumor efficiency. Body weights and survival rates of mice observations over a period of 18 and 40 days showed no obvious body weight losses in the DOX@Ir-NH_2+NIR and DOX@Ir-TF+NIR groups (Fig. 4F and Fig. S28 in Supporting information), indicating effective synergistic chemotherapy/PDT under NIR irradiation. Besides, Kaplan–Meier plots appeared a watershed at 18 days (Fig. 4H), with extended lifespans in the DOX@Ir-TF nanovesicle-treated group upon NIR irradiation, showcasing the nanovesicle's potent synergistic therapy capabilities.

To compare antitumor capabilities of different nanovesicles from a microscopic perspective, Hoechst/terminal deoxynucleotidyl transferase-mediated dUTP nick-end labeling (TUNEL) immumohistochemical staining and hematoxylin and eosin (H&E) histological staining were further performed on pathological sections of tumor tissues. Tumor biopsies of mice treated with the DOX@Ir-NH_2 and DOX@Ir-TF nanovesicles exhibited diffuse TUNEL fluorescence signals, manifesting an apoptosis of tumor cells caused by ROS-induced DNA damage (Fig. 4I and Fig. S29 in Supporting information). The DOX@Ir-TF group exhibited the highest intensity of Hoechst 33342-marked nuclei (blue) and the TUNEL-labeled cell skeleton (green). This was indicated that the DOX@Ir-TF induced the most cell apoptosis and necrosis, likely due to its selective nuclear entry and preferential cancer cell accumulation. Similarly, H&E staining images of the DOX@Ir-TF group's tumor slices revealed the largest necrotic area and sparsest tumor cells, implying the DOX@Ir-TF's superior antitumor ability, enhanced by TF/TfR2-mediated transport, optimizing endocytosis effect, chemotherapy/PDT. Besides, H&E staining analyses for major organs (heart, liver, spleen, lung, and kidney) in mice treated with Ir-based complexes showed no obvious tissue inflammations or le-

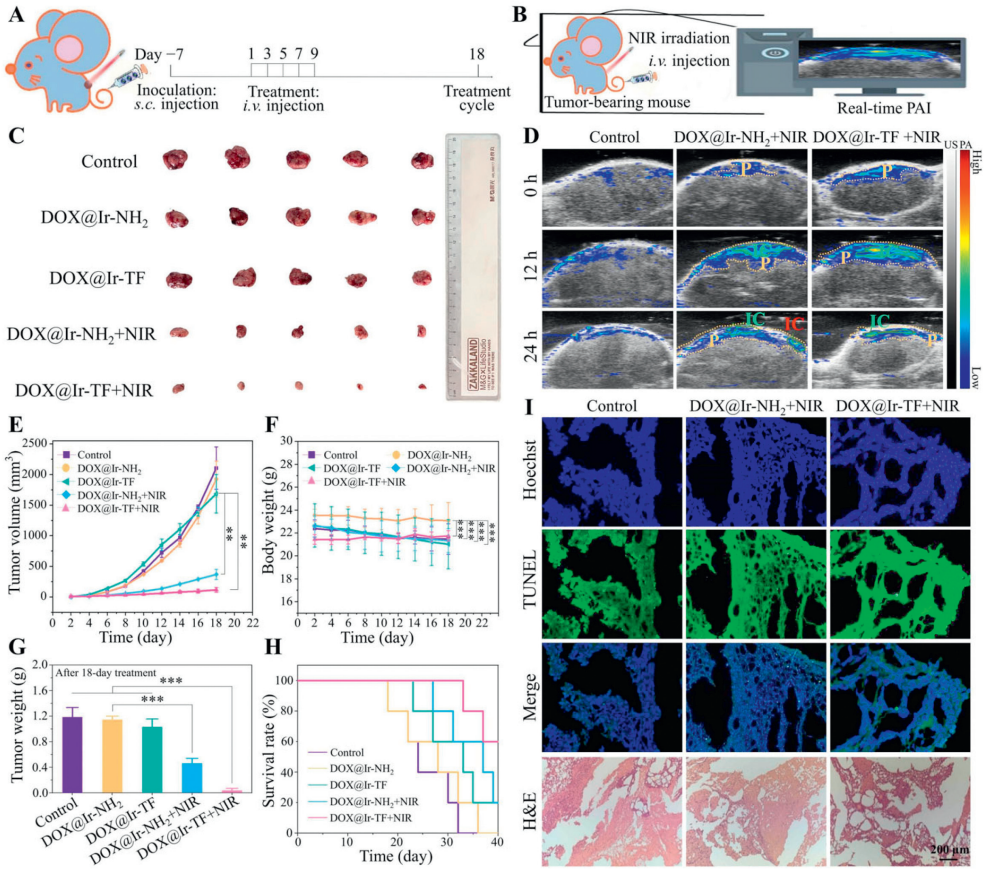

Fig. 4. Antitumor efficacy and PAI monitoring of DOX@Ir-TF *in vivo*. (A) Experimental schedule for DOX@Ir-TF-mediated therapy towards tumor-bearing mice under NIR irradiation. (B) PAI profile to monitor DOX@Ir-TF nanovesicle in the subcutaneous tumors of mice after an irradiation. (C) Photographs of tumor tissues isolated from tumor-bearing mice in different groups at day 18 post-injection. (D) PAI monitoring of tumors after injection of different nanovesicles within 24 h (IC, inflammatory cells; P, PAI signals). (E) Tumor volume changes, (F) body weight changes, and (G) tumor weight changes of mice in different groups. (H) Survival rates of tumor-bearing mice in different groups over a period of 40 days. (I) Representative Hoechst/TUNEL immunostaining and H&E histological staining images of tumor slices from mice in different groups. Scale bar: 200 μm. All statistical data are presented as mean ± SD ($n = 5$; $^{**}P < 0.01$, $^{***}P < 0.001$).

sions (Fig. S30 in Supporting information), manifesting biosafety and potential application of the synthesized DOX@Ir-TF nanovesicle.

In addition to achieving efficient therapeutic effects on tumors, our proposed Ir-based complexes also owned capability of real-time monitoring of tumor progress, thus realizing integrated functionalities of diagnosis and subcutaneous treatment for hepatocellular carcinoma. PAI combines ultrasound's spatial resolution with optical imaging's sensitivity, enabling deep tissue penetration visualization (Fig. 4B). *In vivo* PAI signal changes (Fig. 4D) revealed extensive signals in the DOX@Ir-TF group 12 h post-injection, indicating successful tumor site accumulation due to TF-targeting. Quantitative PAI analyses (Fig. S31 in Supporting information) observed a decrease in signals across all groups at 24 h post-injection, aligning with the NIR/GSH dual-responsive release behavior of DOX. Thus, the DOX@Ir-TF nanoplatform facilitated NIR/GSH dual-responsive drug release and TF-navigated PAI, unveiling promising synergistic chemotherapy/PDT effect towards hepatocellular carcinoma.

In brief, the DOX@Ir-TF nanovesicle designed for PAI-guided synergistic chemotherapy/PDT, exhibited high photo-stability, photoluminescence, and robust ROS production. TF modification on the nanovesicle enhanced tumor cell targeting and uptake efficiency, while QA groups and disulfide-bridged bonds provided NIR/GSH-stimuli responsiveness for controlling drug release at tumor sites. Injection of the nanovesicle into tumor-bearing mice demonstrated significant antitumor effects in a subcutaneous hepatocellular carcinoma model. This synergistic therapy approach combined with PAI functionality, allowed for monitoring *in vivo* tumor therapy in real-time and achieving rapid diagnostic analysis. In brief, this study offers a promising strategy for developing multifunctional Ir-based nanocomposites for efficient subcutaneous hepatocellular carcinoma therapy.

Declaration of competing interest

The authors declare that they have no known competing financial interests or personal relationships that could have appeared to influence the work reported in this paper.

Acknowledgments

This work was financially supported by the National Key R&D Program of China (Nos. 2022YFB3808000, 2022YFB3808001), the Project for High-Level Talent Innovation and Entrepreneurship of Quanzhou (No. 2022C016R), the Medical Innovation Project of Science and Technology Program of Fujian Provincial Health Commission (No. 2021CXA006), and the Key Program of Qingyuan Innovation Laboratory (No. 00221002). The authors also gratefully acknowledged the kind financial support provided by the Top Young Talents of Foal Eagle Program of Fujian Province to Jin Zhang.

Supplementary materials

Supplementary material associated with this article can be found, in the online version, at doi:10.1016/j.cclet.2024.109537.

References

[1] Y.F. Sun, L. Wu, Y. Zhong, et al., Cell 184 (2021) 404–421.
[2] V. Arndt, M. Tim, S. Gonzalo, et al., Lancet 400 (2022) 1345–1362.
[3] X.N. Yu, Y. Deng, G.C. Zhang, et al., ACS Appl. Mater. Interfaces 12 (2020) 17193–17206.
[4] X. Zhao, J. Liu, J. Fan, et al., Chem. Soc. Rev. 50 (2021) 4185–4219.
[5] S. Yi, Z. Lu, J. Zhang, et al., ACS Appl. Mater. Interfaces 11 (2019) 15276–15289.
[6] L.B. Ke, F.M. Wei, L.N. Xie, et al., Angew. Chem. 134 (2022) e202205429.
[7] Y. Qin, F. Tong, W. Zhang, et al., Adv. Funct. Mater. 31 (2021) 2104645.
[8] P. Kaspler, S. Lazic, S. Forward, et al., Photochem. Photobiol. Sci. 15 (2016) 481–495.
[9] M.J. Ye, Y. Gao, M.Y. Liang, et al., Chin. Chem. Lett. 33 (2022) 4197–4202.
[10] G.Q. Yang, Y. Liu, J.J. Chen, et al., Acc. Mater. Res. 3 (2022) 1232–1247.
[11] X.D. Xue, H.J. Qu, Y.P. Li, Exploration 2 (2022) 20210134.
[12] S. Kumar, P. Singh, R. Srivastava, et al., J. Mater. Chem. C 2 (2014) 6637–6647.
[13] M.V. Dwivedi, R.K. Harishchandra, O. Koshkina, et al., Biophys. J. 106 (2014) 289–298.
[14] F.L. Quéméner, D. Subervie, F. Morletsavary, et al., Angew. Chem. Int. Ed. 57 (2018) 957–961.
[15] Y.C. Liu, Y.C. Xie, Y.N. Cheng, et al., Chem. Eng. J. 455 (2022) 140747.
[16] J. Zhao, K. Yan, G. Xu, et al., Adv. Funct. Mater. 31 (2020) 2008325.
[17] X. Sun, J. Zhang, C. Yang, et al., ACS Appl. Mater. Interfaces 11 (2019) 11865–11875.
[18] L. Smeller, K. Solymosi, J. Fidy, B. Böddi, Biochim. Biophys. Acta 1651 (2003) 130–138.
[19] J.J. Chen, Z.Y. Jiang, Y.S. Zhang, et al., Appl. Phys. Rev. 8 (2021) 041321.
[20] S. Grimme, S. Ehrlich, L. Goerigk, J. Comput. Chem. 32 (2011) 1456–1465.
[21] A. Sharma, P. Sudhindra, N. Roy, P. Paira, Inorg. Chim. Acta 513 (2020) 119925.
[22] B. Ni, H. Cao, C. Zhang, et al., Inorg. Chem. 59 (2020) 13671–13678.
[23] Z.X. Fan, Y. Rong, T. Sadhukhan, et al., Angew. Chem. Int. Ed. 134 (2022) e202202098.
[24] H.H. Hu, Z. Zhang, Y.F. Fang, et al., Chin. Chem. Lett. 34 (2023) 107953.
[25] M.D. Kleven, S. Jue, C.A. Enns, Biochemistry 57 (2018) 1552–1559.
[26] U. Kanwal, N.I. Bukhari, N.F. Rana, et al., Int. J. Nanomed. 14 (2019) 1–15.
[27] H.M.A. Zeeshan, G.H. Lee, H.R. Kim, H.J. Chae, Int. J. Mol. Sci. 17 (2016) 327.
[28] Y. Feng, H.X. Zhang, X.X. Xie, et al., Mater. Today Bio 14 (2022) 100288.
[29] Q. Wang, F. Shaik, X.X. Lu, et al., Acta Biomater. 155 (2023) 575–587.